Tunable Catalysis by Reversible Switching Between Ru (III) Single Sites and Ru 0 Clusters in Solid Micelles

Qiyan Wang, Catarina de Brito Mendes, Olga Safonova, Walid Baaziz, César Urbina-Blanco, Dan Wu, Maya Marinova, Ovidiu Ersen, Mickael Capron, Andrei Khodakov, et al.

Tunable Catalysis by Reversible Switching Between $Ru^{(III)}$ Single Sites and Ru^0 Clusters in Solid Micelles

Qiyan Wang,[a#] Catarina M. De Brito Mendes,[b#] Olga V. Safonova,[c] Walid Baaziz,[d] César A. Urbina-Blanco,[b] Dan Wu, [a] Maya Marinova,[e] Ovidiu Ersen,[d] Mickael Capron,[a] Andrei Y. Khodakov, [a]Mark Saeys,[b] Vitaly V. Ordomsky [a]**

[a] *Univ. Lille, CNRS, Centrale Lille, ENSCL, Univ. Artois, UMR 8181 – UCCS – Unité de Catalyse et Chimie du Solide, F-59000 Lille, France;*

[b] *Laboratory for Chemical Technology (LCT), Department of Materials, Textiles and Chemical Engineering, Ghent University, Technologiepark 125, 9052 Ghent, Belgium;*

[c] *Paul Scherrer Institute, CH-5232 Villigen, Switzerland*

[d] *IPCMS, UMR 7504 CNRS, Université de Strasbourg, 23 rue du Loess, BP 43-67034 Strasbourg Cedex 2, France;*

[e] *Institut Chevreul, FR2638 CNRS, Bât. C6 Université Lille 1, F-59655 Villeneuve d'Ascq, France ;*

[#] *equal contribution*

ABSTRACT

Traditionally, catalytic active sites are robust; they do not change after a reaction. We show here that the $Ru^{(III)}$ active sites in a solid micellar $Ru^{(III)}$@MCM catalyst can be controllably switched to Ru^0 nanoclusters and *vice versa* by a mild treatment. The $Ru^{(III)}$ single-sites selectively catalyze the hydrogenation of functional groups such as carbonyl, and double and triple bonds in aromatic compounds via heterolytic H_2 activation. The Ru^0 nanoclusters in contrast are very active for hydrogenating aromatic rings. Ru^0 nanoclusters are reversibly formed from the $Ru^{(III)}$ sites via hydrolysis and reduction as shown by XAS, HRTEM, CO adsorption, and DFT calculations.

The reported strategy offers reversible switching between oxidized and metallic states of Ru to perform different chemical transformations, achieving on-demand active sites.

KEYWORDS: Ruthenium, Solid Micelles, Single-site, Cluster, Switching Catalysis, Arene hydrogenation

1. Introduction

Catalytic active sites are typically rather robust and do not change the oxidation state easily catalyzing only one type of reaction. The reversible switching of active sites from catalyzing one reaction to catalyzing another reaction is therefore rarely observed.

Inspired by nature, switchable catalysis relies on the use of light, pH, coordination events, redox reactions, mechanical forces, or changes in reaction conditions to control a specific chemical transformation [1-3]. Several examples of such "switchable catalysts" can be found in polymerization catalysis [4-7]. Peeck et al. demonstrated switchable stereocontrol in a ring-opening metathesis polymerization (ROMP) reaction by using a pH-sensitive ruthenium-based catalyst [8]. Neutral and protonated ruthenium complexes were tested for norbornene ROMP. The protonation of the amino-substituted NHC (N-heterocyclic carbenes) catalyst ligands led to a significant change in the double-bond geometry of the resulting polynorbornene, showing how the addition of acid allows controlling the ratio between different stereoisomers in the product.

Following a different strategy, Wang et al. reported a range of zirconium- and titanium-based catalysts containing ferrocene-based ligands, able to selectively catalyze the ring-opening polymerization (ROP) of either L-lactide (LA) or ε-caprolactone (CL)[9]. In their reduced state, the Zr^{IV} and Ti^{IV} complexes promote the ring-opening polymerization (ROP) of LA, but are inactive for ROP of CL. Upon oxidation and formation of the cationic Fe^{III}-containing complexes, ROP of CL proceeded instead.

Another example of switchable polymerization catalysis was introduced by

Romain and Williams[10]. A homogenous di-zinc-based catalyst can bridge the cyclohexene oxide (CHO) ring-opening copolymerization (ROCOP) with CO_2 and the CL ring-opening polymerization (ROP) reactions[10]. In their study, the selectivity to polyesters, polycarbonates, or copoly(ester-carbonates) is determined by the zinc–oxygen functionality at the growing polymer chain end and can be controlled by the addition of exogeneous switch reagents, either CO_2 or epoxide. Based on this discovery, the selective formation of block polymers was demonstrated using mixtures of anhydrides, epoxides, and lactones[11, 12].

In heterogeneous catalysis, stimuli-responsive materials have been used to switch Au-NPs between an active and an inactive state[13, 14]. Leitner and co-workers recently reported a catalytic system able to respond adaptively to the feed gas composition in hydrogenation reactions[15]. Ru nanoparticles immobilized on CO_2-responsive support selectively catalyze furfural acetone hydrogenation to 4-(tetrahydro-2-furyl)butan-2-ol or to 4-(2-furyl)butan-2-ol depending on whether pure H_2 or a H_2/CO_2 mixture is fed. The group of Qiao recently reported a switch of CO_2 hydrogenation from CH_4 to CO over Rh/TiO_2 via encapsulation of Rh nanoparticles by reduction at 600 ºC with exposure of single atoms[16].

The use of calcination in air and reduction in hydrogen to switch metal sites between oxidation states to tune catalyst selectivity was previously reported, but less often reversibility between these sites and the catalytic activity of both sites was demonstrated[17-21]. Corma et al. showed that CHA-encapsulated Pt nanoparticles on amorphous silica disperse into site-isolated Pt atoms upon calcination in air at 550 °C

and that the Pt nanoparticles can be re-formed under an H_2 treatment at 400 °C[20]. In 2018, Li et al. reported that noble metal nanoparticles (Pd, Pt, Au-NPs) can be transformed into thermally stable single atoms (Pd, Pt, Au-SAs) above 900 °C in an inert atmosphere[17]. The single-atom catalysts showed superior activity and selectivity for the semihydrogenation of acetylene. Aitbekova et al. reported that Ru nanoparticles redisperse into single sites at temperatures as low as 210 °C in O_2 at 1 atm and that this treatment leads to a switch in catalytic performance from methanation to preferential CO formation with high selectivity[22]. A heterogeneous catalyst, where the active site can be reversibly switched from catalyzing one reaction to catalyzing another, by switching its coordination or oxidation state under mild conditions (T< 150 °C), has not yet been reported. A key requirement would be that the two states of the active sites have comparable thermodynamic stability and can be interconverted by an external stimulus [23].

Solid micellar catalysts (SOMICs) are a new class of catalytic materials that contain isolated metal ion sites incorporated in the walls of a silica matrix and stabilized by surfactant molecules in the pores [24, 25]. The first example of this class, $Ru^{(III)}$@MCM, contains $Ru^{(III)}$ single sites incorporated into the walls of MCM-41 via Ru-O-Si bonds, and stabilized by a cetyltrimethylammonium (CTA^+) surfactant. $Ru^{(III)}$@MCM was shown to be efficient and selective for the hydrogenation of carbonyl, double and triple bonds in aromatic compounds [24, 25].

Here, we demonstrate that the active sites in $Ru^{(III)}$@MCM can be switched to Ru^0 metallic clusters by reduction with H_2 in aqueous phase. The generated Ru^0 clusters

show high activity for the hydrogenation of aromatic rings, a reaction which is not catalyzed by the $Ru^{(III)}$ sites in the original catalyst. The Ru^0 nanoclusters in turn can be transformed back to the $Ru^{(III)}$ single-sites under mild thermal conditions in an inert gas (**Figure 1**). The developed two-state switching strategy creates opportunities for the design of catalysts with tunable active sites, dedicated to orthogonal catalytic transformations.

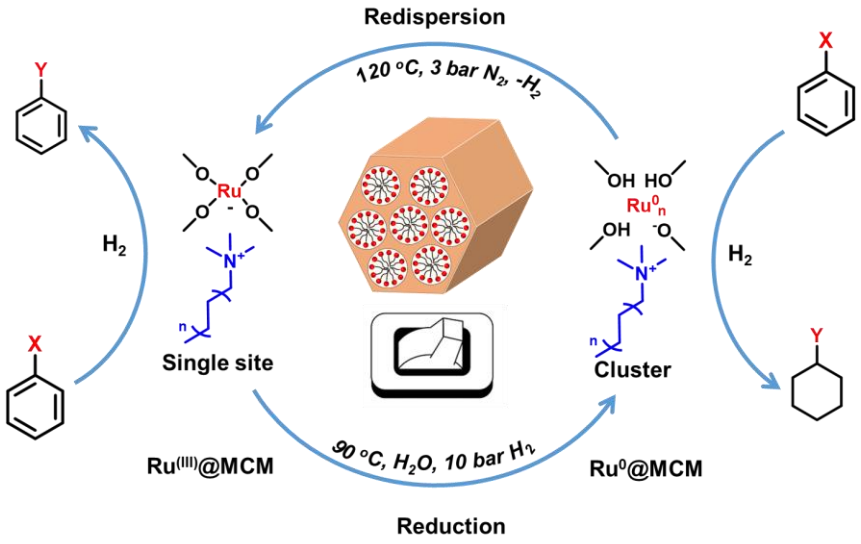

Figure 1. *Illustration of the reversible transformation between $Ru^{(III)}$ single-sites and Ru^0 nanoclusters in the solid micellar catalyst $Ru^{(III)}$@MCM*

2. Experimental section

2.1 Materials

Commercial 5 wt. % Ru/Al_2O_3 catalyst was purchased from Johnson Matthey chemicals company. Ruthenium(III) chloride hydrate ($RuCl_3$, >99.98%), Ammonium chloride (NH_4Cl, >99%), Benzene (C_6H_6, >99.8%), Toluene ($C_6H_5CH_3$, >99.8%), Styrene ($C_6H_5CH=CH_2$, >99%), Phenylacetylene (C_6H_5CH, >98%), Benzophenone ($(C_6H_5)_2CO$, >99%), 2-Methoxyphenol ($C_7H_8O_2$, >99%), Phenol (C_6H_5OH, >99%),

Aniline ($C_6H_5NH_2$, ≥99.5%), p-Phenylenediamine ($C_6H_4(NH_2)_2$, >98%), Benzamide ($C_6H_5CONH_2$, ≥99.5%), 1-Methoxynaphthalene ($C_{10}H_7OCH_3$, >98%), Benzyl phenyl ether ($C_6H_5CH_2OC_6H_5$, 98%), Ethanol (CH_3CH_2OH, ≥99.5%), Ammonia solution ($NH_3 \cdot H_2O$, 25%wt), Tetraethyl Orthosilicate (TEOS, $Si(OC_2H_5)_4$, 98%), Cetyltrimethylammonium Bromide (C_{16}TAB, $C_{19}H_{42}BrN$, >98%) were supplied by Sigma-Aldrich. Argon, nitrogen and hydrogen were supplied by Air Liquide, and were used in the reversible switching of the active sites and catalytic reactions. Deionized water was obtained from a Millipore system. All chemicals have analytic quality and were used without further purification.

2.2. Catalysts synthesis

$Ru^{(III)}$@MCM synthesis starts with the formation of CTAB micelles by adding 1.3 mmol of CTAB to a 96/34 mL deionized water/ethanol mixture, under stirring for 30 mins, until the solution turned clear. After the introduction of $RuCl_3$ to the mixture under continuous stirring for 10 min (CTAB /Ru molar ratio of 3), RuX_4^- ions localize at the interface between the surfactant CTA^+ and the aqueous phase, yielding $Ru^{(III)}$@CTAB. Afterwards, 10 mL 25 wt% aqueous ammonia solution and 2 mL of TEOS were added under continuous stirring for 3 h at room temperature. The resulting solid product $Ru^{(III)}$@MCM was recovered by filtration, washed with water and dried overnight at room temperature.

The sample **$Ru^{(III)}$@MCM-NH_4^+** was prepared by ion exchange of CTA^+ with NH_4^+. 200 mg $Ru^{(III)}$@MCM were mixed with a saturated ammonium chloride solution in ethanol (NH_4Cl/ethanol: 1/50, wt%). This mixture was refluxed at 80 °C for 2 h and

subsequent catalyst separation and washing with ethanol was performed. The procedure was repeated 3 times and the solid was dried afterwards at 80 °C.

The sample **Ru/MCM** was prepared by incipient wetness impregnation of MCM-41 with $RuCl_3$ to provide 5 wt. % of Ru, followed by calcination at 450 °C for 4 h. The catalyst was reduced by H_2 in a fixed-bed reactor at 200 °C for 2 h.

Reduction of the $Ru^{(III)}$@MCM catalyst was conducted in a 40 ml stainless-steel autoclave equipped with a magnetic stirrer, pressure gauge and an automatic temperature controller. In a typical experiment, 1 g of water and 50 mg of catalyst were loaded into the reactor. Then, the reactor was sealed and pressurized with 10 bar of H_2, followed by heating up to 90 °C and continuous magnetic stirring for 1.5 h. The catalysts that underwent this treatment were denoted as **Ru^0@MCM** for the first cycle and **Ru^0@MCM-N** for the following cycles (N).

Redispersion of Ru^0@MCM to **$Ru^{(III)}$@MCM-II** was performed with 3 bar of a N_2 treatment in an autoclave at 120 °C for 4 h. The amount of formed hydrogen was detected by GC analysis.

2.3 Characterization

Transmission Electron Microscopy (TEM) analyses were carried out on a Jeol 2100F (field emission gun) microscope operating at 200 kV and equipped with a probe corrector for spherical aberrations. High angle annular dark field (HAADF)-scanning transmission electron microscopy (STEM) imaging, and energy dispersive X-ray spectroscopy (EDX) of the calcined sample were performed on a double corrected CFEG Jeol-ARM200 transmission electron microscope, operated at 200 kV, using a scanning speed of 20 μs/px for imaging and 0.05 μs/px for EDX for a 0.1 nm probe width and a 120 pA current.

X-Ray Absorption Spectra (XAS) at the Ru K edge were obtained at the Super XAS beamline of the Swiss Light Source (PSI, Villigen, Switzerland). The incident photon beam was selected by a Si (111) channel-cut monochromator from the polychromatic beam coming from a 2.9 T superbend magnet. Rejection of higher harmonics and collimation were achieved by a platinum-coated collimating mirror at 2.5 mrad located before the monochromator, while focusing was achieved by a platinum-coated torroidal mirror at 2.5 mrad. For the detection of Ru K-edge XAS, the beamline was calibrated with metallic Ru (K edge at 22117 eV). The size of the X-ray beam on the sample was about 1.5 mm in horizontal and 0.5 mm in vertical directions. The EXAFS spectra were analyzed using the Demeter software package and the Fourier-transformed k^3-weighted signal was fitted for k = 3-14 $Å^{-1}$ with dk = 1, and R = 1-4 Å with dR = 0.5. The amplitude reduction factor $S_0^2 = 0.81$ was fitted using the metallic Ru reference.

In-situ XAS tests were performed in a quartz capillary with 20 mg of the $Ru^{(III)}$@MCM catalyst. The catalyst was treated in an Ar flow which was switched to H_2 (8 ml min^{-1}) at 10 bar. Temperature was increased from room temperature to 90 °C while recording the spectra. The catalyst was reduced by the injection of water using a syringe pump at 0.4 ml min^{-1} into the H_2 flow under 10 bar for 1.5 h. Redispersion was performed by switching the gas to Ar at atmospheric pressure (8 ml min^{-1}), without water injection, at 90 °C.

FTIR spectra were recorded using a Thermo Fisher Scientific Nicolet 6700 FTIR (32 scans at a resolution of 4 cm^{-1}) equipped with a mercury cadmium telluride detector in a vacuum cell with KBr windows. The sample was evacuated for 1 h ($<10^{-4}$ torr) at 70 °C with the subsequent addition with CO adsorption until saturation at room temperature.

H_2-TPR measurements were conducted in a CryoCooler using a heating rate of 10 ºC/min under a 5% H_2/Ar flow. The wet and dried samples were obtained by treatment of $Ru^{(III)}$@MCM with Ar flow at room temperature and 70 ºC, respectively.

2.4. Computational details

Density Functional Theory (DFT) calculations were performed using Gaussian16. The single Ru active sites were modelled using a cluster containing 17 Si, 32 O, 12 H, and 1 Ru atoms (**Figure S1, SI**). Geometries were optimized using the PBE0[26] functional and the def2-TZVP[27] basis set. Frequency calculations were performed at the same level of theory to compute thermodynamic properties. The bottom part of the cluster model (6 Si, 8 O and 6 H atoms) was kept fixed. The chemical potential for water was obtained from a cluster of four molecules of H_2O. The Gibbs free energy change (ΔG_1, kJ/mol) associated to the hydrolysis of the Ru single sites was calculated according to Eq.5:

$$\Delta G_1 = (G(Ru(OH)_3(H_2O)_3) + G([[17-Si]^-)) - \left(G\left([[Ru^{III}@17-Si]^-\right) + 4\,G(H_2O)\right) \quad (5)$$

For each cluster size and hydrogen coverage of Ru_xH_y (x=2-3, y=0-24), a set of isomers was optimized. For each structural isomer, spin multiplicities from 1 to 9 were considered. All geometries were fully optimized using PBE[28] functional and the def2-TZVP[27] basis set without symmetry constraints to obtain the most energetically stable structures (**Tables S1-S2, SI**). The stability of the Ru_xH_y clusters was estimated by calculating the Gibbs free energy change (ΔG_2, kJ/mol) associated with the reduction of $Ru(OH)_3(H_2O)_3$ by hydrogen (Eq. 2), according to (Eq. 6):

$$\Delta G_2 = 6\,G(H_2O) + \frac{1}{x}G\left(Ru_xH_y\right) - (G(Ru(OH)_3(H_2O)_3) + \left(\frac{3}{2}+\frac{y}{2x}\right) \times G(H_2)) \quad (6)$$

A negative value of ΔG implies a favorable process in which the final species are more stable than the initial ones.

2.5. Hydrogenation reactions

Hydrogenation reactions were conducted in a 40 ml stainless-steel autoclave equipped with a magnetic stirrer, pressure gauge and an automatic temperature controller[29]. In a typical experiment, 1.2 mmol of the substrate has been dissolved in 4 ml of ethanol and 50 mg of the catalyst were loaded into the reactor. Afterwards, the reactor was sealed and pressurized by 10 bar of H_2, followed by heating up to the target temperature with continuous magnetic stirring. After the reaction, the autoclave was cooled down, the pressure was released and the solution was separated by filtration and analyzed by GC (Agilent Technologies 7820A, equipped with an HP-5 capillary column and flame ionization detector) with biphenyl as the internal standard. The products were identified by GC-MS (Agilent Technologies 5977A MSD with Agilent Technologies 7890B GC system equipped with an HP-5 capillary column).

The conversion, the selectivity and the product yield were defined as follows:

$$\text{Conversion}\ (\%) = 1 - \frac{n_A}{n_A^0} \quad (8)$$

$$\text{Selectivity to the product, p}\ (\%) = \frac{n_p}{(n_A^0 - n_A)} \quad (9)$$

$$\text{Yield}\ (\%) = \text{Conversion} \times \text{Selectivity} \quad (10)$$

where n_A and n_A^0 refer to the final and the initial number of moles of reactant, respectively. n_p is the number of moles of converted reactant to the product *p*.

3. Results and discussion

3.1. Reversible transformation between $Ru^{(III)}$ single-sites and Ru^0 clusters

The synthesis of $Ru^{(III)}$@MCM catalyst was described previously[24, 25]. Briefly, micelles are formed from cetyltrimethylammonium bromide (CTAB), EtOH and H_2O. After the introduction of $RuCl_3$, $Ru^{(III)}$ ions localize at the interface between the surfactant micelles and the aqueous phase. Hydrolysis of tetraethoxysilane (TEOS) around the micelles creates a solid MCM-41-type material with isolated $Ru^{(III)}$ sites incorporated in the silica walls and stabilized by the CTA^+, surfactant with a Ru content of 3.2 wt. % (**Figure 1**). STEM-HAADF micrographs show the well-defined hexagonal arrangement and uniform pore structure characteristic of MCM-41 (**Figure 2, Figure S2, SI**). Using high-magnification STEM-HAADF, the metal distribution in the silica matrix was identified. Small bright spots (<1 nm) in the walls of $Ru^{(III)}$@MCM correspond to the Ru single-site species, as confirmed by elemental mapping (**Figure S3, SI**).

The electronic state and coordination of Ru in $Ru^{(III)}$@MCM were studied by X-ray absorption spectroscopy (XAS). The $Ru^{(III)}$@MCM XANES spectrum (**Figure 3** and **Figure S4-S5, SI**) shows that Ru in the $Ru^{(III)}$@MCM is in an oxidized state, according to the reference of RuO_2 and $RuCl_3$. Fourier transform (FT) EXAFS moduli (**Figure S6, SI**) can be fitted for Ru atoms coordinated by 4.2 ± 0.5 oxygen neighbours at 2.1 ± 0.1 Å (**Table S3, SI**), and without Ru-Ru coordination, consistent with isolated $Ru^{(III)}$ species incorporated in the silica walls of MCM-41 (**Figure 1**). When the gas was switched to H_2, no changes corresponding to reduction $Ru^{(III)}$ were observed in the spectra by heating to 90 °C (**Figure S7, SI**). It is worth noting that the introduction of water flow together with H_2 caused a gradual decrease in the Ru white line intensity,

(**Figure 3a**) pointing towards a gradual reduction of $Ru^{(III)}$ [30]. K-edge EXAFS-FT moduli confirm the decrease in the Ru-O scattering intensity and the appearance of Ru-Ru scattering (**Figure 3b**).

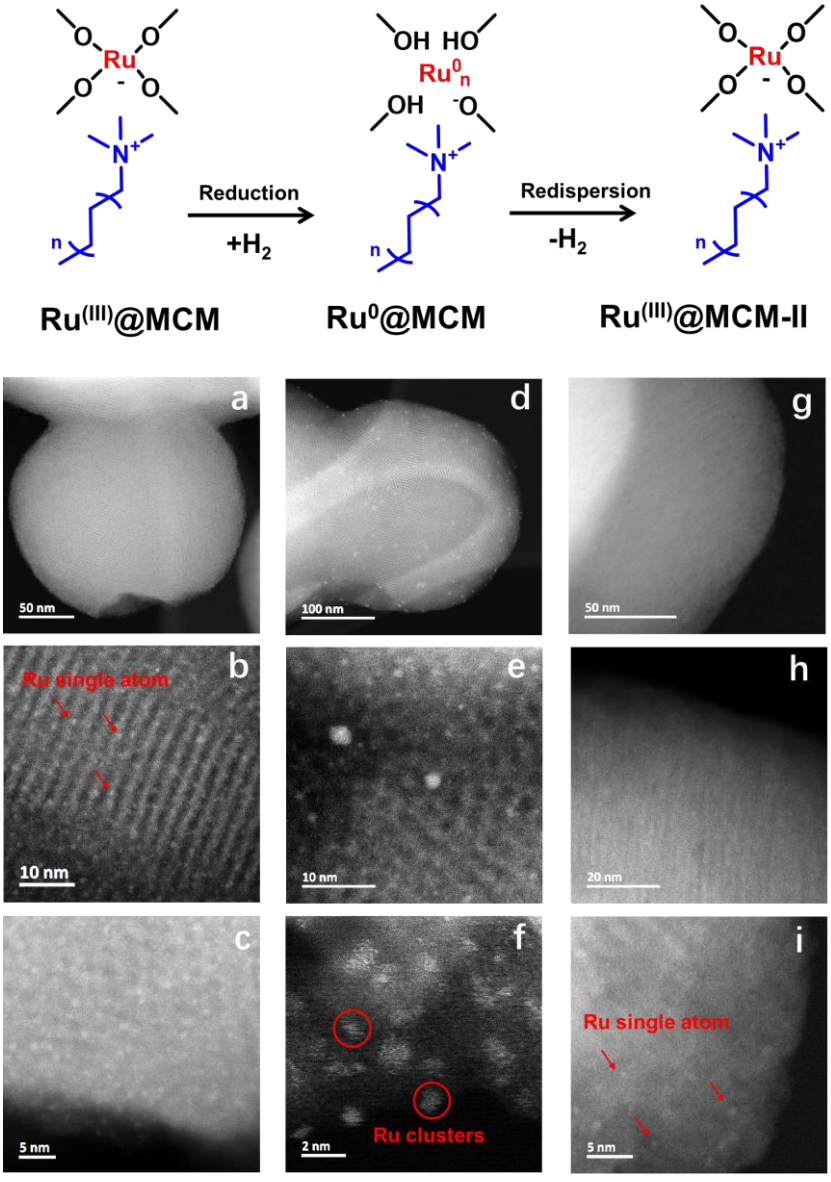

Figure 2. *TEM and STEM-HAADF images at different scale of the initial $Ru^{(III)}$@MCM catalyst (a-c), Ru^0@MCM after reduction in H_2 in the presence of water (d-f), and $Ru^{(III)}$@MCM-II after redispersion treatment in an inert atmosphere (g-i).*

After 3 h under reducing aqueous conditions, EXAFS modeling shows a Ru-Ru coordination of 3.5 ± 1.4 at a typical Ru^0-Ru^0 distance of 2.7 ± 0.02 Å (**Table S3, Figure**

S6, SI). In addition, the results obtained from H_2-TPR confirmed a fast reduction of $Ru^{(III)}$ at low temperature over $Ru^{(III)}$@MCM in the presence of water in comparison with slow reduction under dry conditions (**Figure S8, SI)**. The formation of 0.2-1.0 nm Ru nanoclusters is also observed in STEM-HAADF micrographs of a sample prepared by exposing $Ru^{(III)}$@MCM to 10 bar hydrogen and aqueous conditions in a batch reactor at 90 °C (**Figure 2, Figure S9, SI**). The observed clusters appear highly amorphous and are uniformly distributed within the pores of MCM-41.

Next, switching the atmosphere in the capillary to a pure Ar flow at the same temperature resulted in a gradual increase in the white line intensity in the XANES spectrum, a decrease of the peak related to Ru-Ru scattering and an increase of the peak related to Ru-O scattering in the EXAFS spectra, suggesting redispersion of the Ru nanoclusters (**Figure 3**).

TEM analysis of the sample prepared by treatment of Ru^0@MCM in N_2 in a batch reactor at 120 °C, which is higher than in XAS test, and elemental mapping confirmed the disappearance of the nanoclusters and showed single sites distributed in the walls of MCM-41 (**Figure 2, Figure S10, SI**).

It was recently reported that supported noble metal nanoparticles can be transformed into single atoms by treatment in an inert gas at high temperatures of 900 °C [17] (**Table S4, SI**). Here, the redispersion of Ru in SOMIC materials is performed under much milder conditions by a simple change of the gas from hydrogen to argon. CTA^+ seems to play a key role in this transformation by stabilizing $Ru^{(III)}$ single sites, but also by isolating small Ru^0 clusters to suppress sintering. The strong interaction

between $Ru^{(III)}$ and CTA^+ sites can be observed by the high stability of CTA in the pores of $Ru^{(III)}$@MCM compared with the easy extraction of surfactant from Ru-free MCM in ethanol (**Figure S11, SI**). To evaluate the role of CTA^+, the surfactant was exchanged with NH_4^+, forming $Ru^{(III)}$@MCM-NH_4^+. The IR results revealed the absence of any peaks associated with C-H vibrations after the exchange (**Figure S12, SI**). Reduction of this catalyst resulted in the formation of metal nanoparticles between 3 and 5 nm (**Figure S13, SI**). Switching to an Ar atmosphere did not redisperse the Ru nanoparticles (**Figure S14, SI**), highlighting the importance of the CTA^+ surfactant.

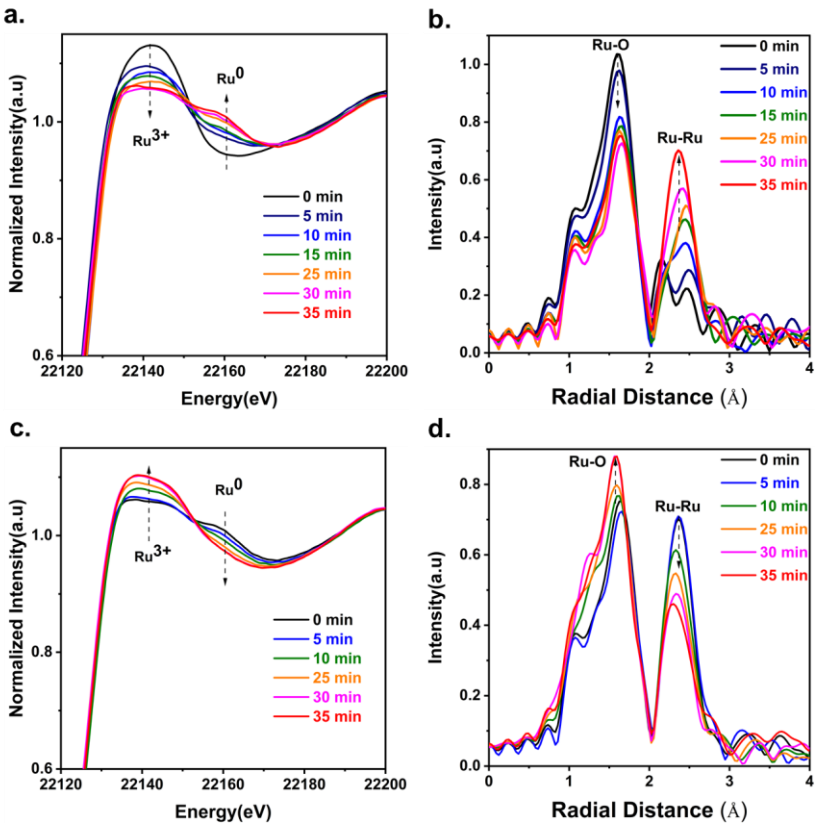

Figure 3. *In-situ XANES and EXAFS spectra of the Ru K-edge for $Ru^{(III)}$@MCM during reduction in 10 bar H_2, H_2O at 90 °C (a, b) and during redispersion in 1 bar flowing Ar at 90 °C (c, d).*

3.2. Switchable catalysis: hydrogenation of functionalized arenes

According to the literature, small metallic Ru^0 nanoclusters are highly efficient for the hydrogenation of aromatic compounds (**Table S5, SI**). Toluene hydrogenation at 40 °C and 10 bar hydrogen was selected as a model reaction to contrast the performance of the Ru^0@MCM catalyst with that of its parent $Ru^{(III)}$@MCM. $Ru^{(III)}$@MCM showed very low activity with a toluene conversion of only 7 % after 1.5 h in a batch reactor (**Figure 4**). Switching from the $Ru^{(III)}$@MCM catalyst to Ru^0@MCM by a mild reduction in the presence of water created a highly active catalyst with a toluene conversion above 80% under the same conditions (**Figure 4**). Redispersion of the Ru nanoclusters by treating the catalyst in an inert atmosphere for 3 h switched the SOMIC catalyst back to the $Ru^{(III)}$@MCM state, as illustrated by the low toluene hydrogenation activity (<10% conversion after 1.5 h) (**Figure 4**). This cycle could be repeated several times, demonstrating the bistability of our catalytic system. The excellent low temperature aromatic hydrogenation activity of Ru^0@MCM was confirmed for a range of aromatic molecules such as benzene, toluene, phenol, 2-methoxyphenol, benzamide and benzyl phenyl ether (**Figure 4)**. Ru^0@MCM outperformed reference catalysts with similar Ru loading prepared by impregnation of Ru salts on Al_2O_3 (Ru/Al_2O_3) and MCM-41 (Ru/MCM) (**Figure S15, SI**). The superior activity is likely related to the high dispersion of the Ru^0 nanoclusters in Ru^0@MCM. Indeed, the size of the Ru nanoparticles in Ru/MCM prepared by impregnation is in the expected range of 2-5 nm (**Figure S16, SI**).

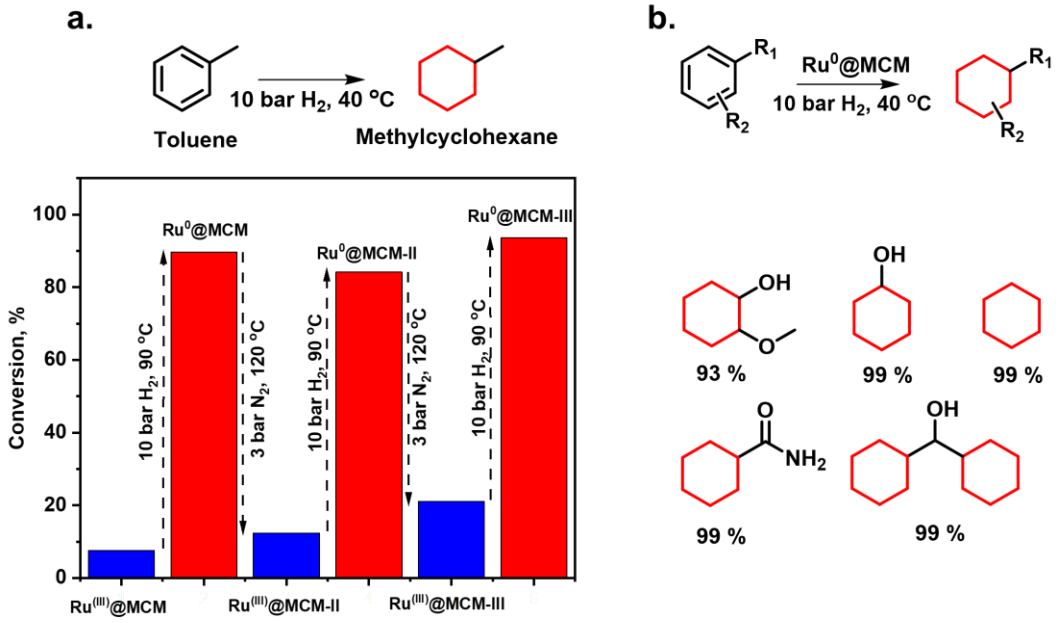

Figure 4. *Switching catalysis. Toluene hydrogenation over the SOMIC catalyst, which is controllably switched from the inactive Ru$^{(III)}$@MCM state to the active Ru^{0}@MCM state via consecutive reduction and redispersion (a) and scope of Ru^{0}@MCM for the hydrogenation of aromatic molecules (yield) (b). (Substrates/ethanol: 1.2 mmol/4 ml, 40 °C,1.5h for Toluene and Benzene, 5h for others,10 bar H_2, 50 mg cat).*

Replacing CTA^+ with NH_4^+ in Ru$^{(III)}$@MCM significantly reduces the reversibility between the Ru$^{(III)}$ and the Ru^0 state (**Figure S17, SI**). As expected, Ru$^{(III)}$@MCM-NH_4^+ shows low activity for toluene hydrogenation. After reduction and formation of Ru^0 nanoparticles, almost full conversion of toluene is observed in 1.5 h (**Figure S17, SI**). Treatment in an inert atmosphere reduces the toluene hydrogenation activity of the catalyst, however, it is significantly higher than for the original Ru$^{(III)}$@MCM-NH_4^+ catalyst. A subsequent reduction again increases the toluene hydrogenation activity, but

much less than for the SOMIC catalyst with the CTA^+ surfactant, illustrating the role of the surfactant in creating a switchable catalyst system.

To ensure that the presence of CTA^+ in the pores does not lead to intra-particle mass transfer limitations[31], and that our experiments were performed under a kinetically controlled regime, the Weisz-Prater, φ, criterion was calculated (**Table S6, SI**). According to this criterion, if the ratio between the observed reaction rate and the diffusion rate is ≤ 1, the internal diffusion resistance can be neglected[32]. The value obtained was 1.11×10^{-1}, which demonstrates that pore diffusion limitations can be disregarded.

To further demonstrate the switching in the nature of the active sites, we selected reactions that are selectively catalyzed by the $Ru^{(III)}$ active sites. At ambient conditions, the $Ru^{(III)}$ sites hydrogenate phenyl acetylene to styrene (62%) and ethylbenzene (37%), without hydrogenating the aromatic ring (**Figure 5**). Under the same reaction conditions, the Ru^0@MCM state of the catalyst hydrogenates phenyl acetylene to ethyl cyclohexane. Hydrogenation of styrene selectively forms ethylbenzene over $Ru^{(III)}$@MCM and ethylcyclohexane over Ru^0@MCM. Hydrogenation of benzophenone over $Ru^{(III)}$@MCM formed diphenylmethanol by hydrogenation of the carbonyl group (**Figure 5**), while over Ru^0@MCM only fully saturated dicyclohexylmethanol was obtained.

In order to exclude the catalytic activity of traces of Ru^0 in $Ru^{(III)}$@MCM sample reduced in the presence of traces of water, the catalytic tests of styrene hydrogenation have been performed in the presence of CO, which should affect the activity of metallic

Ru^0 in comparison with $Ru^{(III)}$. Our results show no effect of CO on the hydrogenation activity of $Ru^{(III)}$@MCM with suppression of hydrogenation activity of Ru^0@MCM (**Figure S18, SI**). Besides, the variation of reaction time shows different selectivity behavior during hydrogenation of styrene over $Ru^{(III)}$@MCM and Ru^0@MCM (**Figure S19-S20, SI**). Ru^0@MCM demonstrates a significant contribution of ethylcyclohexane (30 %) in the product even at low conversions in comparison with the selective synthesis of ethylbenzene for $Ru^{(III)}$@MCM. It excludes an explanation about the same type of metallic Ru^0 sites responsible for catalysis in both Ru^0@MCM and $Ru^{(III)}$@MCM catalysts.

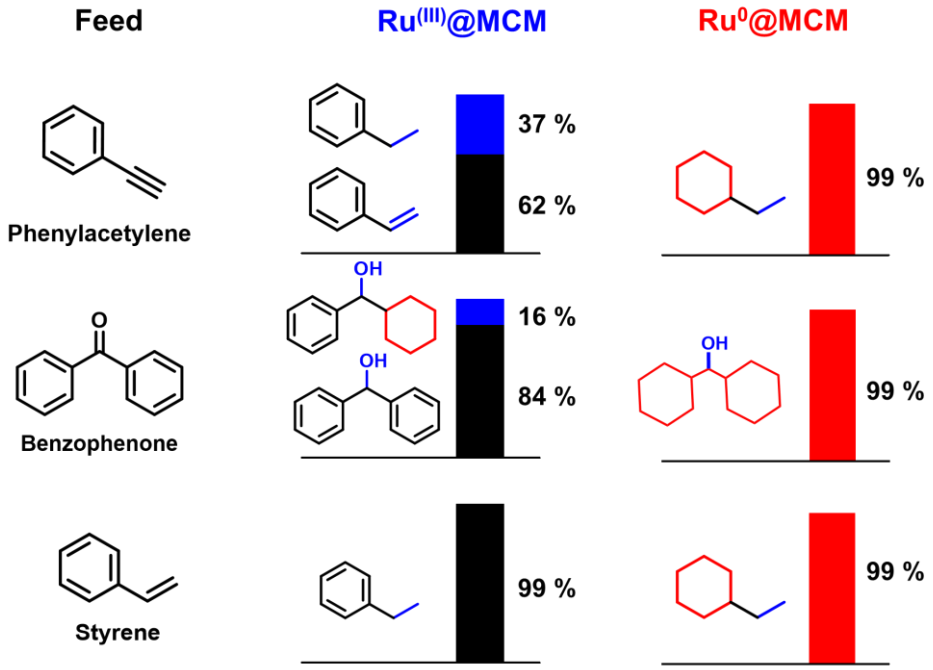

Figure 5. *Switching catalysis. Diverging yield in the hydrogenation of substituted aromatic compounds over $Ru^{(III)}$@MCM and over Ru^0@MCM. Conditions: Substrates/ethanol: 1.2 mmol/4 ml, 40 °C, 1.5h for Styrene and Phenylacetylene, 5h for Benzophenone, 10 bar H_2, 50 mg cat.*

3.3. Mechanism of the reversible transformation between $Ru^{(III)}$ single-sites and Ru^0 nanoclusters

The mechanism of the reversible transformation between $Ru^{(III)}$ single-sites and Ru^0 nanoclusters was analyzed by a series of techniques. Since water is required for the transformation, we postulate that the transformation starts with the hydrolysis of $Ru^{(III)}$-OSi bonds, forming $Ru^{(III)}$ hydroxide complexes and silanol groups, followed by the condensation and reduction of the Ru hydroxide complexes into metallic Ru^0 nanoclusters (Eq. 1-2).

$$[Ru^{(III)}\text{-}(OSi)_4]^-CTA^+ + 3\ H_2O \rightleftharpoons Ru^{(III)}(OH)_3 + 3\ (Si\text{-}OH)_3(SiO^-)(CTA^+) \quad (1)$$

$$Ru^{(III)}(OH)_3 + H_2 \rightleftharpoons \frac{1}{n} Ru^0{}_n(OH) + 2\ H_2O \quad (2)$$

The direct reduction of $Ru^{(III)}$ sites to metallic Ru could be hindered by the stability of $Ru^{(III)}$ species in the walls of MCM-41. Previous studies have indeed shown that H_2 activation is the rate-determining step for hydrogenation reaction over $Ru^{(III)}$@MCM[24]. The transformation of metallic Ru^0 clusters back to $Ru^{(III)}$ single-sites in an inert atmosphere could proceed via oxidation of the Ru nanocluster by silanol groups, accompanied by the release of hydrogen (**Figure 1**). We, therefore, analyzed changes in the state of Ru and hydrogen generation during the transformation.

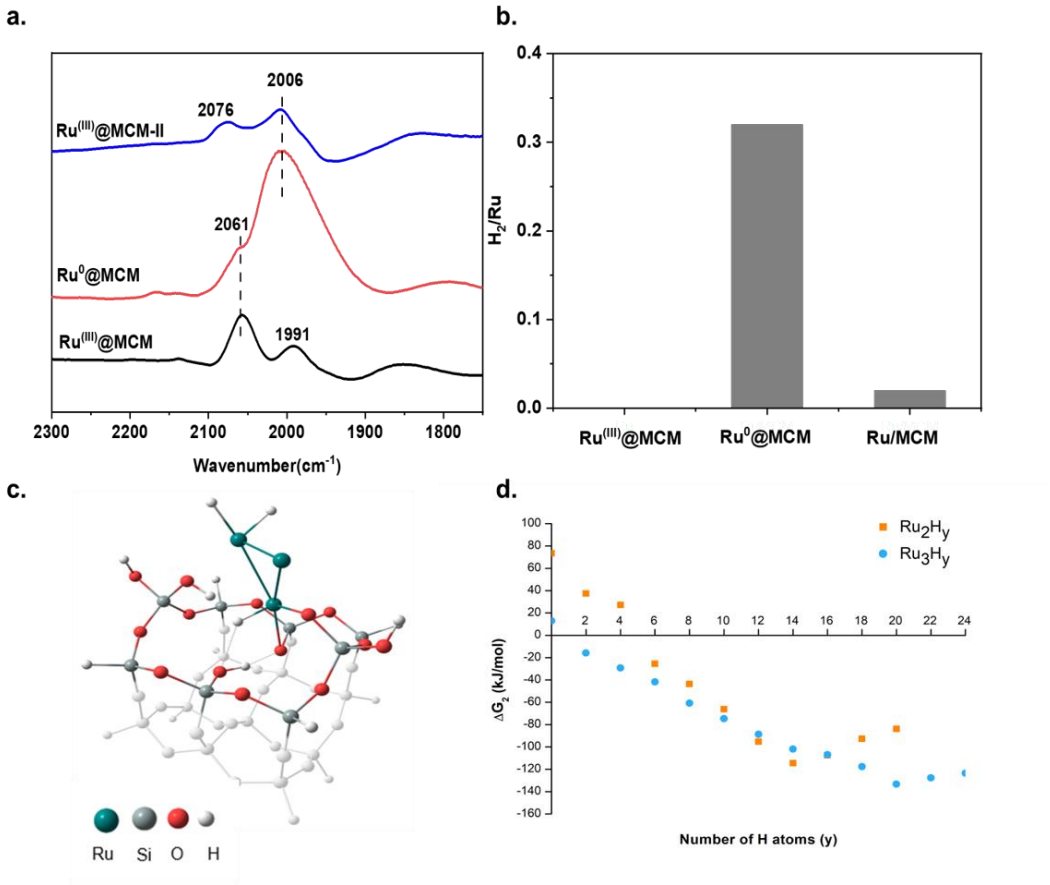

Figure 6. *FTIR spectroscopy of CO adsorption of $Ru^{(III)}$@MCM, Ru^{0}@MCM and $Ru^{(III)}$@MCM-II (a); hydrogen analysis of the inert gas after treatment of $Ru^{(III)}$@MCM, Ru^{0}@MCM and Ru/MCM in N_2 atmosphere at 120 °C (b), representation of the Ru_3H_2 cluster at the MCM-41 surface (c) and Gibbs free energy change (ΔG_2, kJ/mol, Equation 6) of Ru_2H_y and Ru_3H_y cluster formation as a function of the hydrogen coverage (d). DFT calculations were performed in the gas phase with PBE/def2-TZVP at 90°C.*

The generation of hydrogen (and water) during thermal treatment of the Ru^{0}@MCM catalyst in an inert atmosphere in a batch reactor is consistent with the transformation to $Ru^{(III)}$@MCM (**Figure 6**). No hydrogen was detected when $Ru^{(III)}$@MCM was exposed to the same conditions, as expected. The amount of

hydrogen, 0.64 H/Ru, is lower than the stochiometric 3H/Ru (**Figure 1**), likely because not all $Ru^{(III)}$ in the sample is transformed to Ru^0 nanoclusters, and the Ru^0 nanoclusters are only partially reduced. The activity of not converted $Ru^{(III)}$ sites, in this case, will not affect the selectivity over Ru^0@MCM because $Ru^{(III)}$ can hydrogenate only functional groups and Ru^0 functional groups and aromatic rings. Thus, the catalytic switch will be provided if some fraction of Ru can be converted reversibly.

Thermal treatment of the conventional impregnated Ru/MCM catalyst did not generate significant amounts of H_2 since no oxidation and dispersion of the larger Ru nanoparticles is expected in the absence of a stabilizing surfactant.

CO-FTIR spectra also confirmed the transformation of the $Ru^{(III)}$ single sites into Ru^0 nanoclusters (**Figure 6**). CO-FTIR spectra for $Ru^{(III)}$@MCM are characterized by weak band at 2061 cm^{-1}, which can be assigned to CO adsorbed over Ru in ionic state. Transformation to Ru^0@MCM results in the appearance of an intense band at 2006 cm^{-1}, typical for linear CO adsorption on Ru clusters [33]. Subsequent thermal treatment in a vacuum decreases the intensity of the band at 2006 cm^{-1}, leading to a spectrum somewhat similar to the initial spectrum.

DFT calculations further support the two-step reduction of $Ru^{(III)}$ sites to Ru^0 nanoclusters. Direct reduction of $Ru^{(III)}$@MCM to $Ru^{(III)}$-hydride and Si-OH group is highly unfavorable with a standard Gibbs free reaction energy of 133 kJ/mol (**Figure S21, SI**). Hydrolysis of the SiO-$Ru^{(III)}$ bonds (Eq. 3) is more favorable with a positive Gibbs free reaction energy of 60 kJ/mol. The positive Gibbs free reaction energy is consistent with the stability of the $Ru^{(III)}$@MCM catalyst in aqueous conditions.

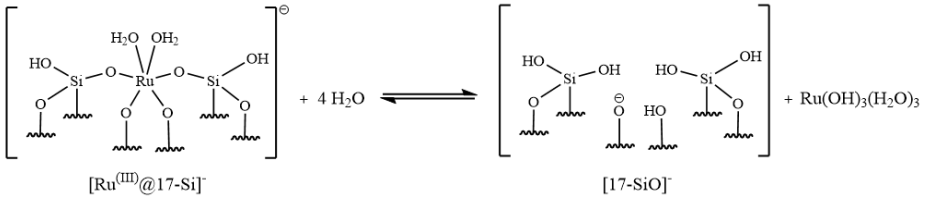

(3)

Subsequent condensation and reduction of the $Ru(OH)_3(H_2O)_3$ complexes in the presence of H_2 drives the formation of Ru^0 nanoclusters stabilized by hydrogen adsorption, and the release of water (Eq. 4).

$$Ru(OH)_3(H_2O)_3 + \left(\frac{3}{2} + \frac{y}{2x}\right) H_2 \rightleftharpoons \left(\frac{1}{x}\right) Ru_xH_y + 6\, H_2O \qquad (4)$$

While the formation of naked Ru_2 and Ru_3 metal clusters from Ru-hydroxide and hydrogen is unfavorable (**Figure 6**), such small clusters can be stabilized by the adsorption of hydrogen, as previously reported [34-36]. The gain in the stability of the hydrogenated clusters reaches a maximum at a critical hydrogen coverage, which depends on the type of metal and size of the cluster considered. In **Figure 6d** the Gibbs free reaction energy for the formation of Ru_2 and Ru_3 clusters is plotted as a function of the hydrogen coverage (Eq 4). Ru_2 clusters require at least six hydrogen atoms to make a reaction (Eq. 4) exergonic, while 2 hydrogen atoms are sufficient for Ru_3 clusters. To allow the reversible transformation of Ru_xH_y clusters back to $Ru^{(III)}$ single-sites, the Ru_xH_y clusters should not be too stable. The size of the nanoclusters inferred from the EXAFS coordination number and the TEM images is moreover somewhat larger than the clusters that were modelled here. While this simple model illustrates the role of water and H_2, it ignores the effect of the surfactant and the SiO^- groups in the walls. The Ru nanoclusters likely interact with the newly formed Si-OH groups, which

compete with H_2 for surface sites, as illustrated in **Figure 6c**. The redispersion of Ru clusters back to $Ru^{(III)}$ should proceed by their reaction with silanol groups. The presence of SiO^- stabilized by CTA^+ could be important for the first nucleophilic attack of Ru cluster to form Ru-O-Si species. It explains why NH_4^+ substituted catalyst is significantly less reversible for this type of switching.

4. Conclusions

$Ru^{(III)}$ single sites incorporated in the walls of MCM-41 and stabilized by quaternary ammonium surfactant can be controllably transformed into metallic Ru^0 nanoclusters by mild reduction in the presence of water. Surprisingly, the resulting metallic Ru^0 nanoclusters can be converted back to single $Ru^{(III)}$ sites by mild treatment in an inert atmosphere, creating a switchable heterogeneous catalyst. The reversible transformation was characterized by XAS, HRTEM, CO-FTIR and DFT calculations and follows a two-step process: hydrolysis of the $Ru^{(III)}$ sites to $Ru(OH)_3$ and silanol groups, subsequent condensation and reduction to Ru^0 nanoclusters. Re-oxidation of Ru^0 nanoclusters proceeds by reaction with silanol groups, generating hydrogen and $Ru^{(III)}$ sites.

$Ru^{(III)}$ sites and Ru^0 nanoclusters demonstrate orthogonal catalytic activities. Ru^0 clusters are highly efficient for the hydrogenation of aromatic rings while $Ru^{(III)}$ single-sites shows high selectivity for the hydrogenation of functional groups such as carbonyl, double and triple bonds in aromatic molecules. The reversible switching between $Ru^{(III)}$ single sites and Ru^0 clusters in solid micelles allows tunable synthesis of aromatic molecules with selectively hydrogenated functional groups or fully hydrogenated

molecules over single-sites and cluster sites, respectively.

Acknowledgments

Vitaly Ordomsky and Qiyan Wang thank the ANR (France) Nano4FUT (ANR-16-CE06-0013) project for financial support. Catarina M. De Brito Mendes, César A. Urbina-Blanco and Mark Saeys acknowledge the support from FWO with the SBO project CATCO_2RE (project number S004118N) and from UGent High-Performance Computing (HPC). The computational resources (Stevin Supercomputer Infrastructure) and services used in this work were provided by the VSC (Flemish Supercomputer Center), funded by Ghent University, FWO and the Flemish Government – department EWI. César A. Urbina-Blanco acknowledges financial support from a senior postdoctoral fellowship from the Fund for Scientific Research Flanders (FWO). We also acknowledge financial support from the 3i University Network with the project "Development of new solid micellar catalysts (SOMIC) for CO_2 hydrogenation to methanol".

References

[1] R.S. Stoll, S. Hecht, Artificial Light-Gated Catalyst Systems, Angewandte Chemie International Edition, 49 (2010) 5054-5075.

[2] V. Blanco, D.A. Leigh, V. Marcos, Artificial switchable catalysts, Chemical Society Reviews, 44 (2015) 5341-5370.

[3] N. Das, C. Maity, Switchable aqueous catalytic systems for organic transformations, Communications Chemistry, 5 (2022) 115.

[4] S.M. Guillaume, E. Kirillov, Y. Sarazin, J.-F. Carpentier, Beyond Stereoselectivity, Switchable Catalysis: Some of the Last Frontier Challenges in Ring-Opening Polymerization of Cyclic Esters, Chemistry – A European Journal, 21 (2015) 7988-8003.

[5] A.J. Teator, D.N. Lastovickova, C.W. Bielawski, Switchable Polymerization Catalysts, Chemical Reviews, 116 (2016) 1969-1992.

[6] T. van Leeuwen, A.S. Lubbe, P. Štacko, S.J. Wezenberg, B.L. Feringa, Dynamic control of function by light-driven molecular motors, Nature Reviews Chemistry, 1 (2017) 0096.

[7] A.C. Deacy, G.L. Gregory, G.S. Sulley, T.T.D. Chen, C.K. Williams, Sequence Control from Mixtures: Switchable Polymerization Catalysis and Future Materials Applications, Journal of the American Chemical Society, 143 (2021) 10021-10040.

[8] L.H. Peeck, S. Leuthäusser, H. Plenio, Switched Stereocontrol in Grubbs−Hoveyda Complex Catalyzed ROMP Utilizing Proton-Switched NHC Ligands, Organometallics, 29 (2010) 4339-4345.

[9] X. Wang, A. Thevenon, J.L. Brosmer, I. Yu, S.I. Khan, P. Mehrkhodavandi, P.L. Diaconescu, Redox Control of Group 4 Metal Ring-Opening Polymerization Activity toward l-Lactide and ε-Caprolactone, Journal of the American Chemical Society, 136 (2014) 11264-11267.

[10] C. Romain, C.K. Williams, Chemoselective Polymerization Control: From Mixed-Monomer Feedstock to Copolymers, Angewandte Chemie International Edition, 53 (2014) 1607-1610.

[11] Y. Zhu, C. Romain, C.K. Williams, Selective Polymerization Catalysis: Controlling the Metal Chain End Group to Prepare Block Copolyesters, Journal of the American Chemical Society, 137 (2015) 12179-12182.
[12] T. Stößer, G.S. Sulley, G.L. Gregory, C.K. Williams, Easy access to oxygenated block polymers via switchable catalysis, Nature Communications, 10 (2019) 2668.
[13] Q. Zhuang, Z. Yang, Y.I. Sobolev, W. Beker, J. Kong, B.A. Grzybowski, Control and Switching of Charge-Selective Catalysis on Nanoparticles by Counterions, ACS Catalysis, 8 (2018) 7469-7474.
[14] Y. Wei, S. Han, J. Kim, S. Soh, B.A. Grzybowski, Photoswitchable Catalysis Mediated by Dynamic Aggregation of Nanoparticles, Journal of the American Chemical Society, 132 (2010) 11018-11020.
[15] A. Bordet, S. El Sayed, M. Sanger, K.J. Boniface, D. Kalsi, K.L. Luska, P.G. Jessop, W. Leitner, Selectivity control in hydrogenation through adaptive catalysis using ruthenium nanoparticles on a CO2-responsive support, Nature Chemistry, 13 (2021) 916-922.
[16] B. Han, Q. Li, X. Jiang, Y. Guo, Q. Jiang, Y. Su, L. Li, B. Qiao, Switchable Tuning CO2 Hydrogenation Selectivity by Encapsulation of the Rh Nanoparticles While Exposing Single Atoms, Small, 18 (2022) 2204490.
[17] S. Wei, A. Li, J.-C. Liu, Z. Li, W. Chen, Y. Gong, Q. Zhang, W.-C. Cheong, Y. Wang, L. Zheng, H. Xiao, C. Chen, D. Wang, Q. Peng, L. Gu, X. Han, J. Li, Y. Li, Direct observation of noble metal nanoparticles transforming to thermally stable single atoms, Nature Nanotechnology, 13 (2018) 856-861.
[18] X. Zhang, Z. Li, W. Pei, G. Li, W. Liu, P. Du, Z. Wang, Z. Qin, H. Qi, X. Liu, S. Zhou, J. Zhao, B. Yang, W. Shen, Crystal-Phase-Mediated Restructuring of Pt on TiO2 with Tunable Reactivity: Redispersion versus Reshaping, ACS Catalysis, 12 (2022) 3634-3643.
[19] S. Zhang, Y. Li, C. Ding, Y. Niu, Y. Zhang, B. Yang, G. Li, J. Wang, Z. Ma, L.-J. Yu, Atomic Dispersion of Pt Clusters Encapsulated Within ZSM-5 Depending on Aluminum Sites and Calcination Temperature, Small Structures, 4 (2023) 2200115.

[20] M. Moliner, J.E. Gabay, C.E. Kliewer, R.T. Carr, J. Guzman, G.L. Casty, P. Serna, A. Corma, Reversible transformation of Pt nanoparticles into single atoms inside high-silica chabazite zeolite, Journal of the American Chemical Society, 138 (2016) 15743-15750.

[21] J.A. Delgado, C. Claver, S. Castillón, D. Curulla-Ferré, V.V. Ordomsky, C. Godard, Fischer–Tropsch synthesis catalysed by small TiO2 supported cobalt nanoparticles prepared by sodium borohydride reduction, Applied Catalysis A: General, 513 (2016) 39-46.

[22] A. Aitbekova, L. Wu, C.J. Wrasman, A. Boubnov, A.S. Hoffman, E.D. Goodman, S.R. Bare, M. Cargnello, Low-Temperature Restructuring of CeO2-Supported Ru Nanoparticles Determines Selectivity in CO2 Catalytic Reduction, Journal of the American Chemical Society, 140 (2018) 13736-13745.

[23] M. Shetty, A. Walton, S.R. Gathmann, M.A. Ardagh, J. Gopeesingh, J. Resasco, T. Birol, Q. Zhang, M. Tsapatsis, D.G. Vlachos, P. Christopher, C.D. Frisbie, O.A. Abdelrahman, P.J. Dauenhauer, The Catalytic Mechanics of Dynamic Surfaces: Stimulating Methods for Promoting Catalytic Resonance, ACS Catalysis, 10 (2020) 12666-12695.

[24] Q. Wang, S. Santos, C.A. Urbina-Blanco, W.Y. Hernández, M. Impéror-Clerc, E.I. Vovk, M. Marinova, O. Ersen, W. Baaziz, O.V. Safonova, A.Y. Khodakov, M. Saeys, V.V. Ordomsky, Solid micellar Ru single-atom catalysts for the water-free hydrogenation of CO2 to formic acid, Applied Catalysis B: Environmental, 290 (2021) 120036.

[25] Q. Wang, S. Santos, C.A. Urbina-Blanco, W. Zhou, Y. Yang, M. Marinova, S. Heyte, T.-R. Joelle, O. Ersen, W. Baaziz, O.V. Safonova, M. Saeys, V.V. Ordomsky, Ru(III) single site solid micellar catalyst for selective aqueous phase hydrogenation of carbonyl groups in biomass-derived compounds, Applied Catalysis B: Environmental, 300 (2022) 120730.

[26] C. Adamo, V. Barone, Toward reliable density functional methods without adjustable parameters: The PBE0 model, The Journal of Chemical Physics, 110 (1999)

6158-6170.

[27] F. Weigend, R. Ahlrichs, Balanced basis sets of split valence, triple zeta valence and quadruple zeta valence quality for H to Rn: Design and assessment of accuracy, Physical Chemistry Chemical Physics, 7 (2005) 3297-3305.

[28] J.P. Perdew, K. Burke, M. Ernzerhof, Generalized Gradient Approximation Made Simple, Physical Review Letters, 77 (1996) 3865-3868.

[29] D. Wu, W.Y. Hernández, S. Zhang, E.I. Vovk, X. Zhou, Y. Yang, A.Y. Khodakov, V.V. Ordomsky, In Situ Generation of Brønsted Acidity in the Pd-I Bifunctional Catalysts for Selective Reductive Etherification of Carbonyl Compounds under Mild Conditions, ACS Catalysis, 9 (2019) 2940-2948.

[30] X. Wang, W. Chen, L. Zhang, T. Yao, W. Liu, Y. Lin, H. Ju, J. Dong, L. Zheng, W. Yan, X. Zheng, Z. Li, X. Wang, J. Yang, D. He, Y. Wang, Z. Deng, Y. Wu, Y. Li, Uncoordinated Amine Groups of Metal-Organic Frameworks to Anchor Single Ru Sites as Chemoselective Catalysts toward the Hydrogenation of Quinoline, J Am Chem Soc, 139 (2017) 9419-9422.

[31] M.F. Neira D'Angelo, V. Ordomsky, J. van der Schaaf, J.C. Schouten, T.A. Nijhuis, Aqueous phase reforming in a microchannel reactor: the effect of mass transfer on hydrogen selectivity, Catalysis Science & Technology, 3 (2013) 2834-2842.

[32] S. Mondal, H. Malviya, P. Biswas, Kinetic modelling for the hydrogenolysis of bio-glycerol in the presence of a highly selective Cu–Ni–Al 2 O 3 catalyst in a slurry reactor, Reaction Chemistry & Engineering, 4 (2019) 595-609.

[33] D. Wu, Q. Wang, O.V. Safonova, D.V. Peron, W. Zhou, Z. Yan, M. Marinova, A.Y. Khodakov, V.V. Ordomsky, Lignin Compounds to Monoaromatics: Selective Cleavage of C-O Bonds over a Brominated Ruthenium Catalyst, Angew Chem Int Ed Engl, 60 (2021) 12513-12523.

[34] P.S. Petkov, G.P. Petrova, G.N. Vayssilov, N. Rösch, Saturation of Small Supported Metal Clusters by Adsorbed Hydrogen. A Computational Study on Tetrahedral Models of Rh_4, Ir_4, and Pt_4, The Journal of Physical Chemistry C, 114 (2010) 8500-8506.

[35] K. Takahashi, S. Isobe, S. Ohnuki, The stabilization of Fe, Ru, and Os clusters

upon hydrogenation, RSC Advances, 3 (2013) 21841-21847.
[36] G. Sun, P. Sautet, Metastable Structures in Cluster Catalysis from First-Principles: Structural Ensemble in Reaction Conditions and Metastability Triggered Reactivity, Journal of the American Chemical Society, 140 (2018) 2812-2820.